Time-of-flight mass measurements of neutron-rich chromium isotopes up to $N = 40$ and implications for the accreted neutron star crust

Z. Meisel,[1,2,*] S. George,[2,3] S. Ahn,[2,4] D. Bazin,[4] B. A. Brown,[4,5] J. Browne,[2,4,5] J. F. Carpino,[6] H. Chung,[6] R. H. Cyburt,[2,4] A. Estradé,[2,7] M. Famiano,[6] A. Gade,[4,5] C. Langer,[8] M. Matoš,[9] W. Mittig,[4,5] F. Montes,[2,4] D. J. Morrissey,[4,10] J. Pereira,[2,4] H. Schatz,[2,4,5] J. Schatz,[4] M. Scott,[4,5] D. Shapira,[11] K. Sieja,[12] K. Smith,[13] J. Stevens,[2,4,5] W. Tan,[1] O. Tarasov,[4] S. Towers,[6] K. Wimmer,[14] J. R. Winkelbauer,[4,5] J. Yurkon,[4] and R. G. T. Zegers[2,4,5]

[1]*Department of Physics, University of Notre Dame, Notre Dame, Indiana 46556, USA*
[2]*Joint Institute for Nuclear Astrophysics, Michigan State University, East Lansing, Michigan 48824, USA*
[3]*Max-Planck-Institut für Kernphysik, 69117 Heidelberg, Germany*
[4]*National Superconducting Cyclotron Laboratory, Michigan State University, East Lansing, Michigan 48824, USA*
[5]*Department of Physics and Astronomy, Michigan State University, East Lansing, Michigan 48824, USA*
[6]*Department of Physics, Western Michigan University, Kalamazoo, Michigan 49008, USA*
[7]*Department of Physics, Central Michigan University, Mount Pleasant, Michigan 48859, USA*
[8]*Institute for Applied Physics, Goethe University Frankfurt a. M., 60438 Frankfurt am Main, Germany*
[9]*Physics Section, International Atomic Energy Agency, 1400 Vienna, Austria*
[10]*Department of Chemistry, Michigan State University, East Lansing, Michigan 48824, USA*
[11]*Oak Ridge National Laboratory, Oak Ridge, Tennessee 37831, USA*
[12]*Université de Strasbourg, IPHC, CNRS, UMR 7178, 67037 Strasbourg, France*
[13]*Department of Physics and Astronomy, University of Tennessee, Knoxville, Tennessee 37996, USA*
[14]*Department of Physics, University of Tokyo, Hongo 7-3-1, Bunkyo-ku, Tokyo 113-0033, Japan*

We present the mass excesses of $^{59-64}$Cr, obtained from recent time-of-flight nuclear mass measurements at the National Superconducting Cyclotron Laboratory at Michigan State University. The mass of ^{64}Cr is determined for the first time, with an atomic mass excess of $-33.48(44)$ MeV. We find a significantly different two-neutron separation energy S_{2n} trend for neutron-rich isotopes of chromium, removing the previously observed enhancement in binding at $N = 38$. Additionally, we extend the S_{2n} trend for chromium to $N = 40$, revealing behavior consistent with the previously identified island of inversion in this region. We compare our results to state-of-the-art shell-model calculations performed with a modified Lenzi-Nowacki-Poves-Sieja interaction in the fp shell, including the $g_{9/2}$ and $d_{5/2}$ orbits for the neutron valence space. We employ our result for the mass of ^{64}Cr in accreted neutron star crust network calculations and find a reduction in the strength and depth of electron-capture heating from the $A = 64$ isobaric chain, resulting in a cooler than expected accreted neutron star crust. This reduced heating is found to be due to the $>$1-MeV reduction in binding for ^{64}Cr with respect to values from commonly used global mass models.

DOI: 10.1103/PhysRevC.93.035805

I. INTRODUCTION

The evolution of nuclear structure away from the valley of β stability is a direct consequence of the forces at work in nuclei [1,2]. Neutron-rich nuclides are of particular interest, since much of the neutron-rich nuclear landscape has yet to be explored [3]. Recently, the experimental reach of radioactive ion beam facilities has extended to chromium for neutron number $N = 40$, where an island of inversion has been inferred from various experimental signatures [4–9]. Trends in first 2^+ excited-state energies $E(2_1^+)$ and ratios between first 4^+ excited-state energies and $E(2_1^+)$ demonstrated a structural change between iron (proton number $Z = 26$) and chromium ($Z = 24$) isotopes near $N = 40$ [4,5,10,11]. This increase in collectivity for chromium near $N = 40$, attributed to a rapid shape change from spherical to deformed structures, is further supported by quadrupole excitation strength $B(E2)$ measurements [6,8,9]. Nuclear mass measurements provide an independent probe of structural evolution which, in contrast to $B(E2)$ measurements, can avoid the bias to proton degrees of freedom [12,13]. Precision mass measurements of manganese isotopes have indicated that the $N = 40$ subshell gap has broken down by $Z = 25$ [7]. However, mass measurements have yet to extend to $N = 40$ in the chromium isotopic chain.

The $N = 40$ chromium isotope ^{64}Cr is of astrophysical interest due to the expected prevalence of $A = 64$ material on the surfaces of accreting neutron stars and, therefore, in the outer neutron star crust [14–16]. The trend in nuclear masses along an isobaric chain strongly impacts the depth and strength of electron-capture reactions that heat and cool the outer crust, altering its thermal profile [17–19]. The resultant thermal profile impacts a host of astronomical observables, including the ignition of type I x-ray bursts [20–22] and superbursts [23,24], the cooling of transiently accreting neutron stars while accretion is turned off [25,26], and, potentially, gravitational wave emission [27,28].

To investigate the open questions in nuclear structure and astrophysics regarding the neutron-rich chromium isotopes,
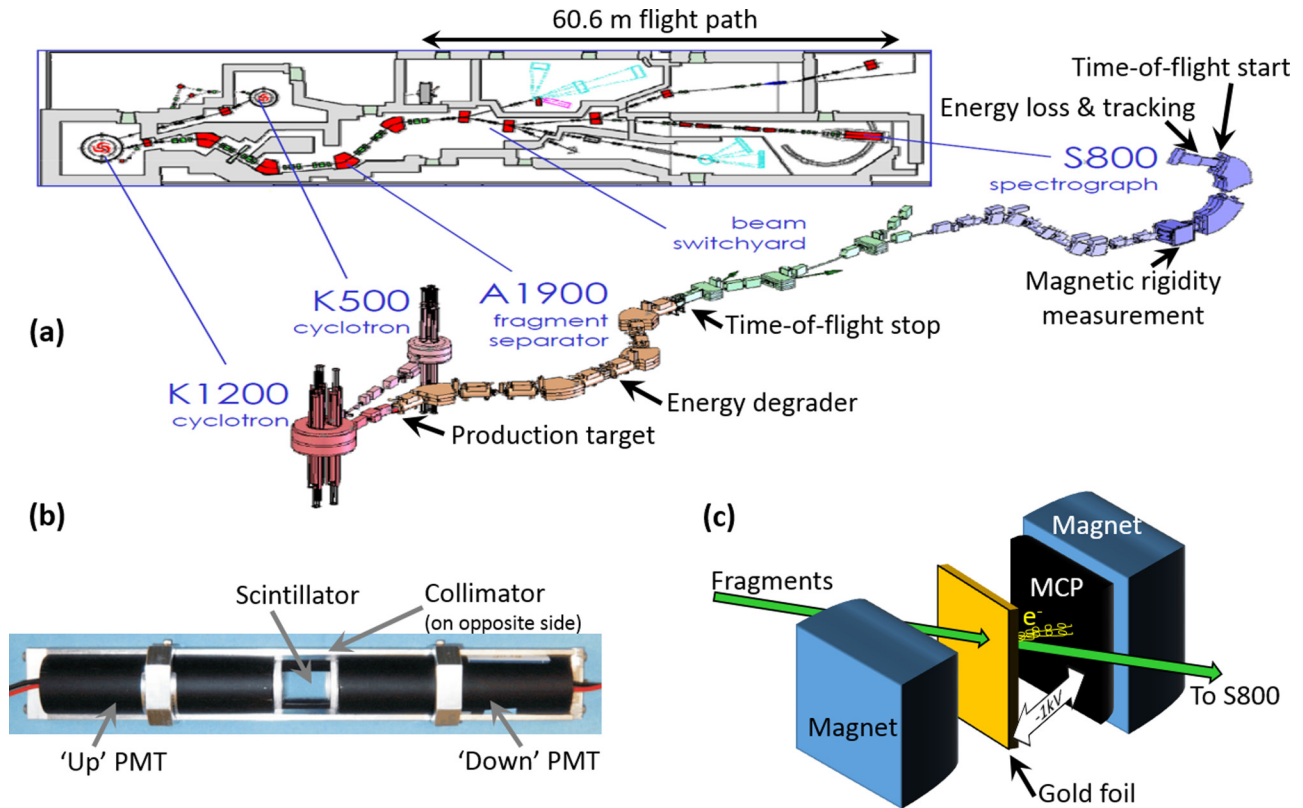
*zmeisel@nd.edu

FIG. 1. (a) Schematic of the NSCL time-of-flight (TOF) mass measurement setup. (b) Scintillator and photomultiplier tube (PMT) pair used to measure TOF stop and start signals at the A1900 and S800 focal planes, respectively. Note that the delayed timing signal from the A1900 was chosen as the stop signal to avoid triggering on events which did not traverse the full flight path. (c) Schematic of the rigidity measurement setup at the target position of the S800. The green arrow represents the beam fragments and the yellow spirals represent the secondary electrons fragments produced by passing through the gold foil, which follow a helical trajectory towards the microchannel plate detector (MCP) due to the -1 kV bias and magnetic field established by the permanent magnets.

we performed time-of-flight (TOF) mass measurements of $^{59-64}$Cr ($Z = 24$, $N = 35-40$) at the National Superconducting Cyclotron Laboratory (NSCL) at Michigan State University. Argon and scandium mass measurements that were a part of the same experiment are discussed in Refs. [13] and [19], respectively. These new chromium masses show significant deviations from the chromium mass trend presented in the 2012 Atomic Mass Evaluation (AME) [29], implying a different structural evolution along the chromium isotopic chain. Our mass measurement of ^{64}Cr extends the mass trend of chromium out to $N = 40$ for the first time. We employ this ^{64}Cr mass in accreted neutron star crust reaction network calculations and, due to the reduction in binding of ^{64}Cr compared to global mass models, find less heating and shallower heating depths than previously expected.

II. EXPERIMENTAL SETUP

A. Time-of-flight mass measurement technique

The masses presented in this work were measured via TOF technique, in which the flight times of ions through a magnetic beam line system are converted to nuclear masses by comparison to the flight times of nuclides with known masses [30]. This technique was chosen due to its ability

to obtain masses for exotic nuclides at the frontier of the known mass surface [18,31]. We employed the TOF mass measurement setup at the NSCL at Michigan State University, described in detail in Ref. [32] and shown in Fig. 1. This setup consists of a 60.6-m flight path between the A1900 fragment separator [33] and the S800 spectrograph [34], with fast-timing detectors located at the A1900 and S800 focal planes, magnetic rigidity $B\rho$ detection at the S800 target position, and energy loss and tracking detectors at the S800 focal plane [35]. About 150 neutron-rich isotopes of silicon to zinc were measured simultaneously over the course of $\sim$100 h.

The Coupled Cyclotron Facility [36] at the NSCL was used to produce a 140 MeV/u ^{82}Se^{32+} primary beam with an intensity of $\sim$30 particle nA, which was fragmented on a beryllium target to produce nuclei of interest. Target thicknesses of 517 mg cm^{-2}, for production of less neutron-rich calibration nuclides, and 658 mg cm^{-2}, for production of more neutron-rich nuclides of interest, were used alternately, keeping the $B\rho$ of the A1900 and S800 fixed. Fragments were transmitted through the A1900 fragment separator [34], where slits reduced the momentum acceptance to $\pm 0.5\%$. A 7.2 mg cm^{-2} Kapton wedge degrader was placed at the intermediate image of the A1900 to remove the high flux of low-Z fragments, which would otherwise have complicated particle identification (PID) and increased data acquisition
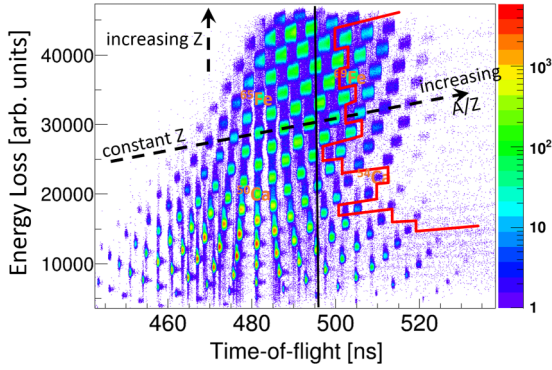
FIG. 2. Particle identification plot of nuclei produced in this time-of-flight (TOF) mass-measurement experiment, where the color indicates the production intensity (counts per 100 ps × 10 ionization-chamber adc units) and the TOF was not rigidity-corrected. Nuclei located on the right of the red line had no known experimental mass prior to the mass measurement reported here; ^{50}Ca, ^{54}Ca, ^{65}Fe, and ^{69}Fe are labeled for reference. The data are from ≈11 h of thin-target production and ≈91 h of thick-target production.

dead time. The S800 analysis line ion optics were set to a dispersion-matching mode to provide a momentum dispersion at the S800 target position of ≈1%/11 cm, which enables an accurate rigidity measurement. This ion optical setting provides an achromatic focus on the timing detectors in the A1900 and S800 focal planes. The full set of nuclei detected over the course of the mass measurement is shown in Fig. 2. Timing and magnetic rigidity determinations are discussed in more detail in Secs. II B and II C, respectively.

The relationship between the TOF and the nuclear rest mass m_{rest} is obtained from the equation of motion for a charged massive particle through a magnetic system. Equating the two counteracting forces, the Lorentz force F_L and the centripetal force F_c, results in the following relationship:

$$F_c = F_L,$$

$$\frac{\gamma(v) m_{rest} v^2}{\rho} = q v B,$$

$$m_{rest} = \frac{1}{v} \frac{q(B\rho)}{\gamma(v)},$$

$$m_{rest} = \frac{TOF}{L_{path}} \frac{q(B\rho)}{\gamma\left(\frac{L_{path}}{TOF}\right)}, \quad (1)$$

where the Lorentz factor γ is a function of the velocity v, which is in turn the ratio of the flight-path length L_{path} to the flight-time TOF. It follows that, in principle, the simultaneous measurement of an ion's TOF, charge q, and $B\rho$ through a system of known L_{path} yields m_{rest}. However, in practice, L_{path} and the ion optical dispersion used to measure $B\rho$ are not known with sufficient precision to obtain a precise value for m_{rest}. Furthermore, it is more practical to make a relative than an absolute measurement of $B\rho$. Instead, the $\frac{m_{rest}}{q}$(TOF) relationship is determined empirically by measuring the TOF of calibration or reference nuclei [30]. The chosen reference nuclei have well-known masses (≲100-keV uncertainty),

have no known isomers with lifetimes comparable to the flight time (∼500 ns), and are as close as possible in nuclear charge Z and mass A to the nuclides of interest in order to minimize systematic uncertainties [30].

Ultimately, TOF was measured for ∼150 nuclides, ranging from atomic number $14 \lesssim Z \lesssim 30$ and atomic mass–to–atomic number (here the ion charge $q = Z$) ratio $2.35 \lesssim A/Z \lesssim 2.72$. The measured TOFs were in the range of ∼500 ± 25 ns. The event-by-event TOFs were corrected for their $B\rho$ variation due to the finite $B\rho$ acceptance of the ion optical system using a globally fit (i.e., fit over the full range of nuclides) correction based on the measured position at the S800 target location. The resultant single-species TOF distributions for the $B\rho$-corrected data were fit with a Gaussian distribution in order to determine a mean TOF for each nuclide. The relationship between mass over charge m_{rest}/q and TOF was fit to the data on reference nuclides in order to ascertain the calibrated m_{rest}/q(TOF) relationship, which was used to obtain the measured masses reported in this work.

B. Timing measurement

The method employed in Ref. [32] was used to measure the TOF for nuclides in the mass measurement reported here. Two BC-418 ultrafast timing scintillators from Saint-Gobain Crystals [37], 1 cm tall × 1.5 cm wide × 0.25 cm thick, were each coupled to two Hamamatsu R4998 [38] 1-in.-diameter photomultiplier tubes (PMTs) housed in an H6533 assembly [see Fig. 1(b)]. One timing detector was installed in the focal plane of the A1900 fragment separator, serving as the stop detector (after including a delay time). The second timing detector was installed in the focal plane of the S800 spectrograph. This choice for start and stop signals prevented triggering the data acquisition system for ions which did not traverse the full flight path. The signal from each PMT was split. One signal was used for timing information and the other signal was used to measure the magnitude of the light output for position and Z information. To maintain signal quality, timing signals were transported to the data acquisition electronics via Belden [39] model 7810A delay cables. This setup provided an intrinsic timing resolution of ∼30 ps [32].

Various combinations were made of the four PMT timing signals, one each from the "up" (low-$B\rho$ side) and "down" (high-$B\rho$ side) PMTs of the A1900 and S800 timing detector setup, to create a TOF for each event, the *event TOF*, each of which is discussed in detail in Ref. [40]. The event TOF which was ultimately chosen to minimize the systematic uncertainty in the final results is the "down-clock" TOF from Ref. [40]. For this event TOF, the high-$B\rho$ PMT signals from the S800 and A1900 fast-timing scintillators were each used to start separate channels of a time-to-amplitude converter (TAC), which each had a stop signal generated by a clock. Each separate TAC time randomly populated the full range of an analog-to-digital converter (ADC), canceling out systematic effects from local nonlinearities in the ADC channel-to-time mapping, which are difficult to characterize and correct. The random time component of the event-TOF timing signals was removed by taking the difference between the two clock times, referred to as $T_{S3D-Clk}$ and $T_{XFU-Clk}$ for the S800 and
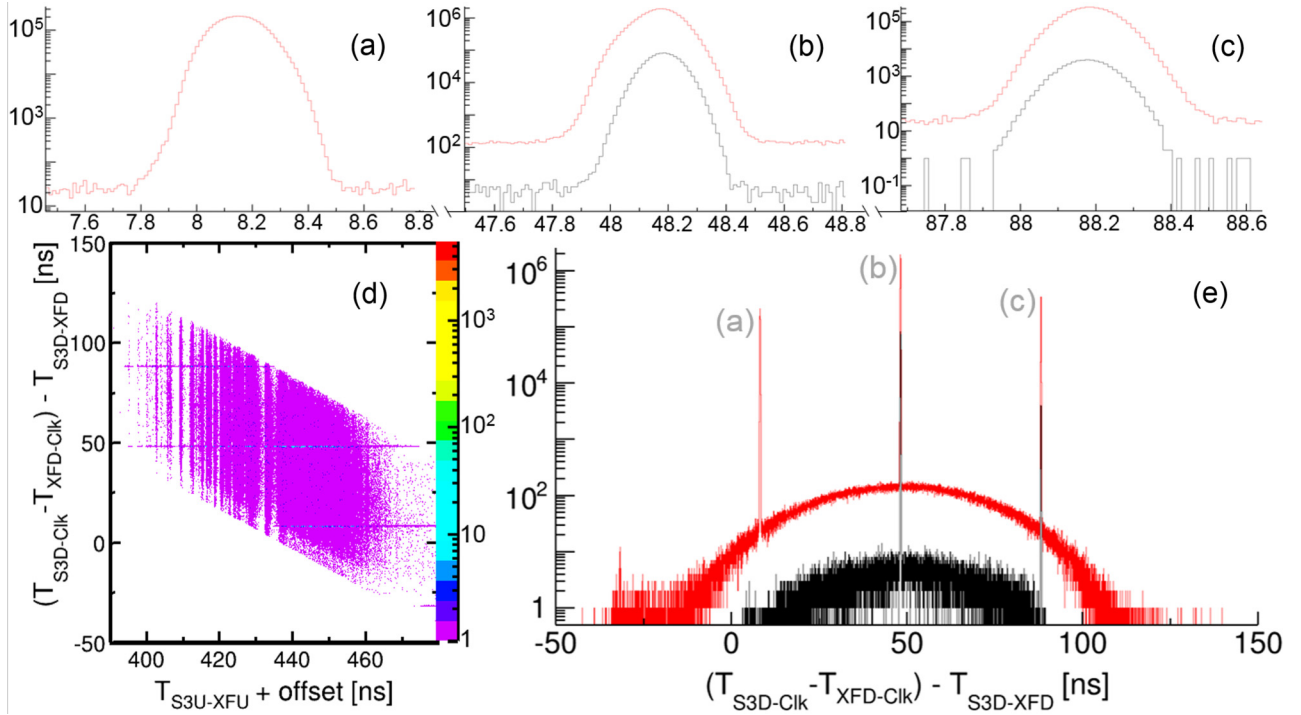
FIG. 3. Spectra employed for the clock pulse correction. The time difference between a direct time-of-flight (TOF) and a clock TOF (e) results in multiple peaks (a–c) spaced by the clock period $T = 40$ ns. Narrow gates around the peaks were used to remove background and to determine the clock pulse correction that was to be added to a given event. (d) Demonstration of the fact that events of an ion with a single direct TOF can result in multiple clock TOFs. The random coincidences which are prominent in (d) are shown in (e) to be a small fraction of the total events. Vertical structures in (d) are due to the fact that ions with similar A/Z values had similar TOFs, where the feature at $\approx$432 ns corresponds to $A/Z = 2.5$. Black histograms in (a)–(c) and (e) are gated on events of ^{45}Ar, the highest statistics isotope observed, while red histograms represent all events.

A1900 low-$B\rho$-side PMT vs clock times, respectively. The event TOF constructed from the clock-stopped time difference, $T_{XFD-Clk} - T_{S3D-Clk}$, for a given flight time could vary by an integer multiple of the clock period ($T = 40$) ns, since the clock pulses came at random intervals with respect to the ion flight-time measurement. The event TOF was corrected for the number of clock pulses via a comparison to the direct TOF measured between the two low-$B\rho$-side PMTs, as shown in Fig. 3. An additional correction was applied to each event TOF to account for the systematic shift associated with an ion's scintillator impact positions, which were obtained from the direct time difference between the opposing PMTs on each of the fast-timing scintillators, $T_{XFU-XFD}$ and $T_{S3U-S3D}$.

The event-by-event TOF for each ion was

$$
\begin{aligned}
\mathrm{TOF}_{event} = {}& T_{XFD-Clk} - T_{S3D-Clk} \\
& + N_d T + \tfrac{1}{2}(T_{XFU-XFD} - T_{S3U-S3D}) + t_{offset},
\end{aligned} \tag{2}
$$

where N_d is the number of clock pulses to correct for (via Fig. 3) and $t_{offset} = 480$ ns is an arbitrary offset applied to bring the measured TOFs closer to the expected true TOFs, which differ due to the chosen delay cable lengths.

C. Rigidity determination

A relative measurement of $B\rho$ was performed using the method developed in Ref. [41] at the target position of the S800 spectrograph, which was operated in a dispersion matched mode [34]. This consisted of sending the ion beam through a foil and guiding the secondary electrons generated in this process to the surface of an 8 cm wide $\times$ 10 cm tall (where the width is along the nondispersive direction) microchannel plate detector (MCP; see Fig. 1). The foil was a 70 μg cm^{-2} polypropylene film sputtered with 1500 Å of gold biased to -1 kV, which provided an electric field to guide electrons directly from the foil to the MCP, the face of which was at ground potential. The MCP consisted of two Quantar [42] model 3398A lead-glass plates oriented in the chevron configuration. Rectangular NdFeB 35 permanent magnets from Magnet Sales and Manufacturing [43] were held coplanar to the foil and MCP by a steel yoke in order to create a region of nearly homogeneous magnetic field between the foil and the MCP, so that the secondary electrons would follow a tight spiral along their flight path. The secondary electrons were multiplied by the MCP in an avalanche which was collected on a resistive back plane, where electrons freely drifted to its four corners. The foil was mounted on a ladder which also contained a foil and a hole mask with a known hole pattern, shown in Fig. 4(a), which was used for the dispersive position ($\propto B\rho$) calibration.
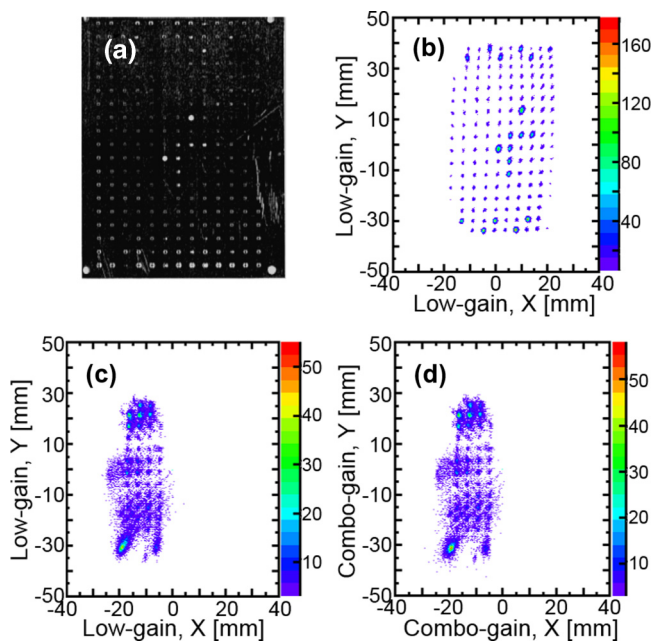
FIG. 4. (a) The mask with a distinctive hole pattern (5-mm hole spacing) which was placed between the incoming ion and the gold foil in order to allow electrons to be created only from certain locations for calibration runs. (b) The image created on the MCP by electrons generated from a ^{232}Th α source. (c, d) The image created by the electrons generated by the ^{82}Se primary beam, where the beam was tuned to four separate positions to achieve the mask coverage shown; the low-gain corner signals were used in (c), and the combined high-low gain signals in (d). Since only the relative position was relevant, the effort was not made to achieve the exact 5-mm hole spacing of the mask in the MCP image.

Ion impact positions on the MCP, and therefore on the foil, were reconstructed by determining the relative amount of charge collected on each corner of the resistive back plane. For a single event, the nondispersive X_{MCP} and dispersive Y_{MCP} positions of an ion at the foil were given by

$$X_{\mathrm{MCP}} = \frac{\mathrm{UR} + \mathrm{LR} - \mathrm{UL} - \mathrm{LL}}{\mathrm{UL} + \mathrm{UR} + \mathrm{LL} + \mathrm{LR}},$$

$$Y_{\mathrm{MCP}} = \frac{\mathrm{UL} + \mathrm{UR} - \mathrm{LL} - \mathrm{LR}}{\mathrm{UL} + \mathrm{UR} + \mathrm{LL} + \mathrm{LR}}, \quad (3)$$

where UL, UR, LL, and LR are the charges collected on the upper left, upper right, lower left, and lower right corners, respectively, of the MCP back plane. Each corner signal was split and sent through low- and high-gain amplifications, which were optimum for positions close to and far from a given corner, respectively. In practice, the positions reconstructed from the low-gain amplification were of comparable quality to the combined-gain positions, as shown in Fig. 4, and so the low-gain corner signals were used for the final MCP position determination. The achieved position resolution was $\sigma \approx 0.5$ mm and $\sigma \approx 1.0$ mm for secondary electrons generated by a ^{228}Th α source and an ^{82}Se primary beam, respectively, where the lower resolution for the primary beam was due to the higher initial kinetic energy of the secondary electrons [44] and, therefore, larger cyclotron radius [45,46].
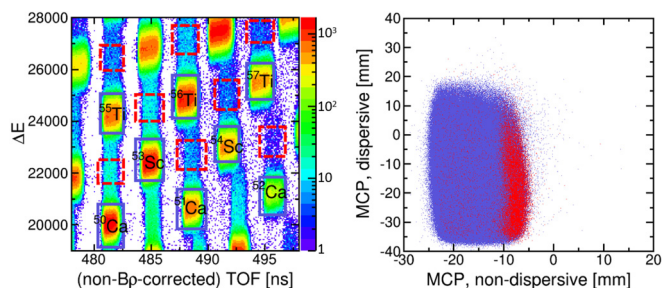

FIG. 5. Demonstration of the correlation between high-energy-loss (ΔE) PID events and the microchannel plate (MCP) nondispersive position. Left: A subset of the PID-containing isotopes of calcium, scandium, and titanium, where "main" events are within the purple boxes and "top-hat" events are within the dashed red boxes. Right: The location of the main (purple dots) and top-hat (red dots) events on the MCP; it is clear that the relatively high-ΔE events corresponded to larger nondispersive positions.

In addition to providing a relative measure of $B\rho$, the MCP position measurements were used to identify scattering on a collimator upstream of the foil that was used to protect the MCP during beam tuning. Scattering on the collimator reduced the energy of the scattered fragment, resulting in an increased energy loss in the S800 focal-plane ionization chamber that was used for PID. These scattered events added a "top hat" feature above the "main" (nonscattered) events in the PID, as shown in Fig. 5. A position gate, $X_{\mathrm{MCP}} < -11$ mm, was applied to remove scattered events from the analysis.

III. DATA ANALYSIS

A. Rigidity correction

Due to the accepted momentum spread of $\pm 0.5\%$, a rigidity correction was required to remove the momentum dependence from the measured TOF spectra. The $B\rho$ correction was first determined individually for each nuclide, the "local" $B\rho$ correction, by fitting the TOF-Y_{MCP} relationship for the set of events belonging to a given nuclide. The parameters of the local rigidity corrections were then fit to determine a smooth variation of these parameters as a function of A and Z, resulting in the "global" $B\rho$ correction, which was ultimately used to momentum-correct the data. The global correction function allows for the momentum correction of nuclides with low statistics, for which a precisely determined local correction was not possible, removes spurious systematic effects from unphysical variations in the local rigidity corrections due to limited statistics, and ensures a consistent treatment of the data when used for all nuclides.

The local $B\rho$ correction was performed isotope by isotope in an iterative fashion. First, the TOF-vs-Y_{MCP} data for an isotope were histogrammed, converted into a graph with ROOT's TPROFILE [47] class, and fit with a linear function (see Fig. 6). A linear function was chosen, as it was found to reduce the overall systematic uncertainty in the final mass fit [40]. The linear dependence of TOF on Y_{MCP} was then removed [see Fig. 6(b)], the data were projected onto the TOF dimension, and the projected histogram was fit with
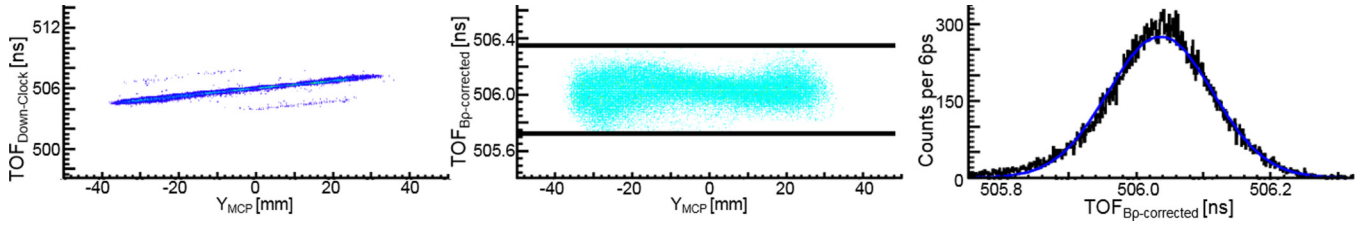
FIG. 6. First iteration of the local $B\rho$ correction for ^{64}Cr. Left: Histogram of TOF vs Y_{MCP} for events identified as ^{64}Cr, which was converted to a graph by applying ROOT's TPROFILE class to the histogram and fit with a linear function. Middle: The resultant $B\rho$-corrected TOF-vs-Y_{MCP} histogram after removal of the linear trend shown in the left panel, pivoting about $Y_{\mathrm{MCP}} = 0$. Right: Projection onto the TOF dimension of the rigidity-corrected (black histogram) TOF-vs-Y_{MCP} relationship, where the blue line is a Gaussian fit. Black lines in the middle panel indicate $\pm 4\sigma$, where σ is the standard deviation of the Gaussian fit of the right panel.

a normal distribution [see Fig. 6(c)]. Due to contamination from misidentified nuclei in the PID, the TOF-vs-Y_{MCP} spectra contained two weak lines parallel to the main linear data trend, offset to higher and lower TOFs, since low-$B\rho$ (low-TOF) events from higher-TOF nuclides could be misidentified as high-$B\rho$ (high-TOF) events from the nuclide of interest, and vice versa for events from lower-TOF nuclides. The $B\rho$ measurement allowed these misidentified nuclei to readily be identified in the TOF-vs-Y_{MCP} spectra, however, they skewed the slope of the initial linear fit. Therefore, following the fit-correction-projection-fit procedure shown in Fig. 6, a cut was made to select only events within 4σ from the TOF centroid of the normal distribution fit. The fit-correction-projection-fit procedure was then repeated until convergence was reached to obtain the slope of the local $B\rho$ correction for that isotope. The linear local $B\rho$ correction was found to be insufficient for isotopes of elements with $Z < 17$ and $Z > 26$ and nuclides with $A/Z < 2.44$, so these nuclides were excluded from the analysis. On average the slope of the TOF-Y_{MCP} relationship was ~ 40 ns mm^{-1}.

The locally determined linear dependencies of the TOF on Y_{MCP} were then fit to determine a global $B\rho$ correction. Various polynomials in A, Z, and A/Z were explored, up to fourth order in each variable, and the optimum fit function in terms of goodness of fit was selected,

$$\left(\frac{d\mathrm{TOF}}{dY_{\mathrm{MCP}}}\right)_{\mathrm{global}} = a_0 + a_1 \frac{A}{Z} + a_2 \left(\frac{A}{Z}\right)^2 + a_3 Z$$
$$+ a_4 Z^2 + a_5 A, \qquad (4)$$

where a_i are fit parameters. The global $B\rho$-correction slopes from this fit reproduced the local $B\rho$-correction slopes within 1%. The same optimum global fit function was found in Ref. [18]. An element-by-element fit to the local $B\rho$-correction slopes was also explored, though it was found to be inferior in terms of the final mass-fit systematic uncertainty [40]. The local, global, and by-element $B\rho$-correction slopes are compared in Fig. 7. Note that isotopes with $Z = 17$ are not shown since they were ultimately excluded from the analysis due to their drastically different behavior in TOF as a function of m/q, as determined by the mass fit. (Recall that isotopes of elements with $Z < 17$ and $Z > 26$ were previously excluded from the analysis due to their poor local $B\rho$ correction determination.)

The global $B\rho$ correction was applied to the TOF spectra, as shown in Fig. 8 for the chromium isotopes, where it is apparent that a shift in the average TOF of the distribution occurs due to the choice of Y_{MCP} about which the TOF was pivoted. The $B\rho$ correction improved the σ_{TOF} from ~ 2 to ~ 0.08 ns. The final TOF for each nuclide was determined by fitting the $B\rho$-corrected TOF with a normal distribution, gating on events within $\pm 4\sigma$ of the TOF centroid, and repeating the fitting-gating procedure until convergence. The statistical uncertainty of the mean TOF for measured nuclides was $\delta\mathrm{TOF} \lesssim 1$ ps, corresponding to a TOF measurement precision of roughly 1 part in 10^6.

B. Mass evaluation

The fit to the mass over charge m/q–TOF surface, referred to elsewhere in this article as the mass fit, consisted of choosing a set of reference nuclides to calibrate the $m_{\mathrm{rest}}/q(\mathrm{TOF})$ relationship, finding the optimum fit function, and assessing the various uncertainties contributing to the final mass results obtained for nuclides that were not used as calibrants. Nuclides chosen as calibrants had a literature experimental mass uncertainty of $\leqslant 50$ keV, as listed in the 2012 AME [29] (except for ^{53}Ca and ^{54}Ca, which come from Ref. [48]), and no isomers longer-lived than 100 ns, as listed in the National Nuclear Data Center database [49]. The 20 nuclides used to calibrate the $m_{\mathrm{rest}}/q(\mathrm{TOF})$ relationship were $^{44-47}$Ar, $^{47-51}$K, $^{49-54}$Ca, ^{63,65,66}Mn, and ^{64,66}Fe. A map of the reference nuclides with respect to the nuclides for which a mass was evaluated is shown in Fig. 9.

The atomic masses from Ref. [29] were corrected to obtain the nuclear masses by subtracting the individual electron binding energies listed in Table II of Ref. [50]. A relativistic correction was applied to the measured TOF for nuclides in order to account for time dilation. Additionally, the average TOF and Z for all nuclides of interest were subtracted from the TOF and Z for each nuclide to create effective time and charge variables, i.e., $\tau = \mathrm{TOF} - \langle\mathrm{TOF}\rangle$ and $z = Z - \langle Z \rangle$, in order to reduce the multicollinearity of the mass-fit parameters [32].

The initial uncertainty in m_{rest}/q ascribed to the data points was the literature mass uncertainty added in quadrature to the statistical uncertainty, where the latter used standard propagation of uncertainty to translate uncertainty in TOF into uncertainty in m/q. This statistical uncertainty depended on the fit function itself, $\delta M_{\mathrm{stat.}} = (\delta\mathrm{TOF}) \times \frac{\partial}{\partial\mathrm{TOF}}(\frac{m}{q}(\mathrm{TOF}))$, where
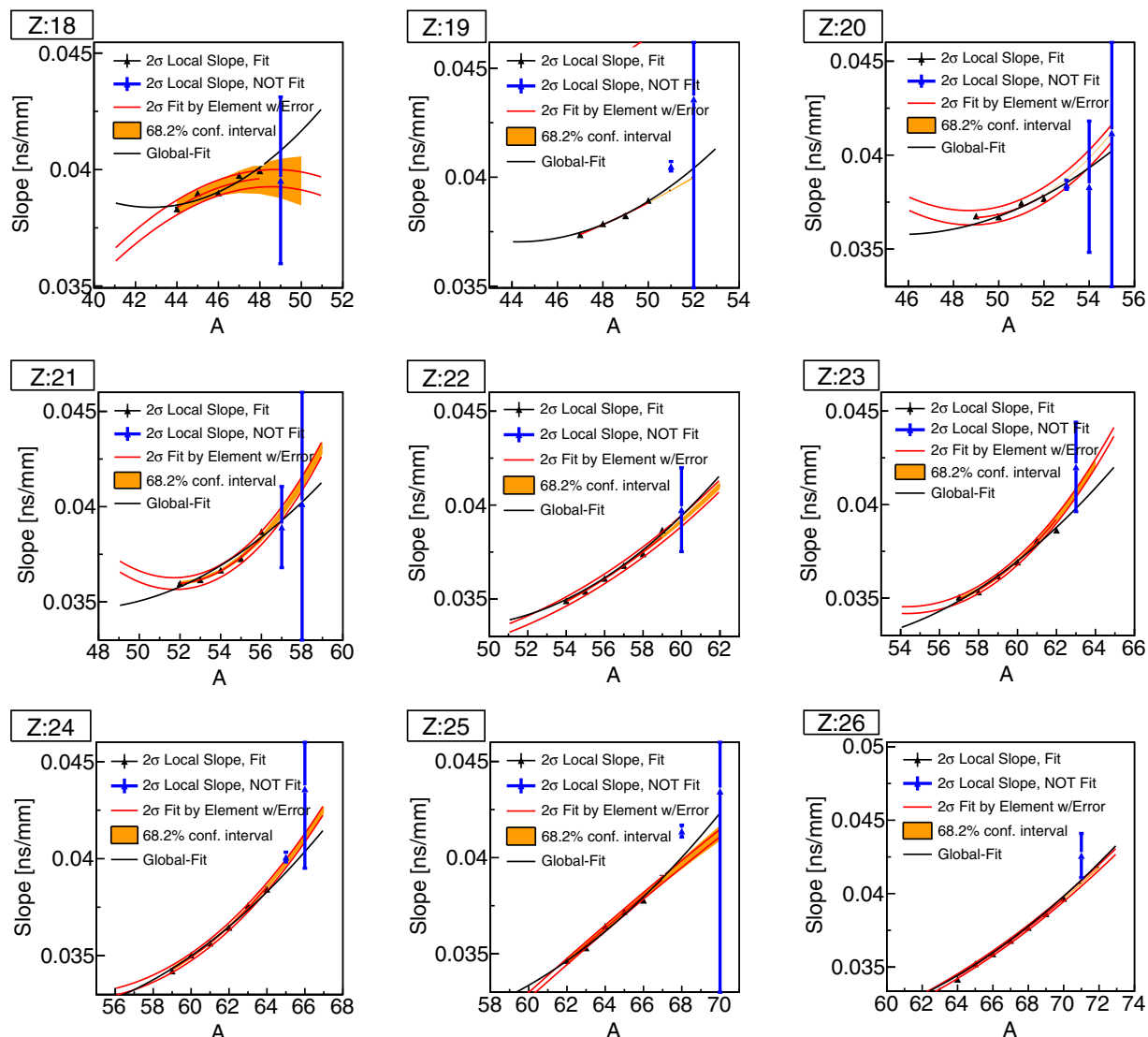
FIG. 7. TOF-vs-Y_{MCP} slope as a function of the mass number A for observed isotopes of argon, potassium, calcium, scandium, titanium, vanadium, chromium, manganese, and iron ($18 \leqslant Z \leqslant 26$), respectively, as determined by "local" by-nucleus fits (data points) and fits to the locally determined slopes that employed the $\pm 2\sigma$ cutoff, where black data points were included in the fit and blue points were not. The by-element fit along a single isotopic chain as a cubic function of A is shown by the red lines; the upper and lower lines indicate the extremes obtained for upper and lower limits of the fit parameters, and the orange band indicates the $\pm 1\sigma$ confidence interval. The black line shows the trend of the rigidity-correction slope along an isotopic chain as determined by the global fit to all locally determined slopes of nuclei with $A/Z > 2.44$ and $18 \leqslant Z \leqslant 26$.

$\frac{m}{q}$(TOF) is the m_{rest}/q(TOF) calibration function and δTOF is the one standard deviation uncertainty of the mean TOF for a nuclide (data point). Therefore, the final statistical uncertainty assigned to each data point was determined in an iterative procedure where the data were fit to obtain a m_{rest}/q(TOF) calibration function, statistical uncertainties were calculated for each of the data points (corresponding to reference nuclides), and the process was repeated until convergence.

Upon completion of the mass fit, including literature and statistical uncertainties, the reduced χ^2 of the fit was typically much larger than 1. This indicated that the uncertainty of the 20 reference nuclide data points was underestimated and that some additional heretofore unaccounted for uncertainty was present. As there were no systematic trends in the fit residuals, we treat the additional uncertainty as a systematic error. The approach outlined in [32] was followed, where the missing uncertainty was treated as a statistically distributed systematic uncertainty, i.e., one that accounted for a uniform scatter in the mass-fit residual as a function of m_{rest}/q. (We note that a similar procedure has been used previously in storage ring isochronous mass spectrometry [51].) Such an effect could have been created by many uncontrolled factors in the measurement, such as time-dependent magnetic field drift of the dipole magnets along the beam line, time-dependent variations in the response of the timing electronics due to variations in temperature, and unidentified biases present in the data analysis pipeline. To include this additional systematic uncertainty, the uncertainty of reference nuclide data points
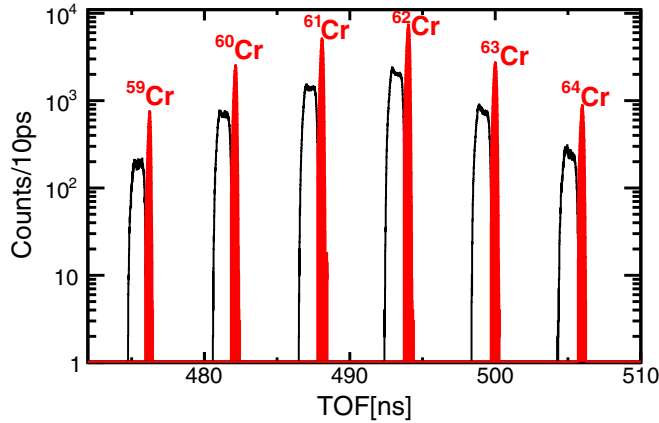
FIG. 8. Time-of-flight (TOF) distribution of chromium isotopes before (open histograms) and after (filled red histograms) the global magnetic rigidity correction.

was increased uniformly, i.e., each data point had the same systematic uncertainty $\delta M_{\rm syst.}$ (in keV q^{-1}), until $\chi^2_{\rm red.} = 1$. We note that the results for the mass fit with and without inclusion of the systematic uncertainty agreed within the final one-standard-deviation uncertainty. The mass fit was then repeated and the statistical uncertainty was recalculated to be consistent with the current parameters of the fit function. This process was then repeated iteratively until it converged. The fit function resulting from this procedure was the $m_{\rm rest}/q$(TOF) calibration function, which was used to obtain the masses of noncalibration nuclides whose TOF was measured.
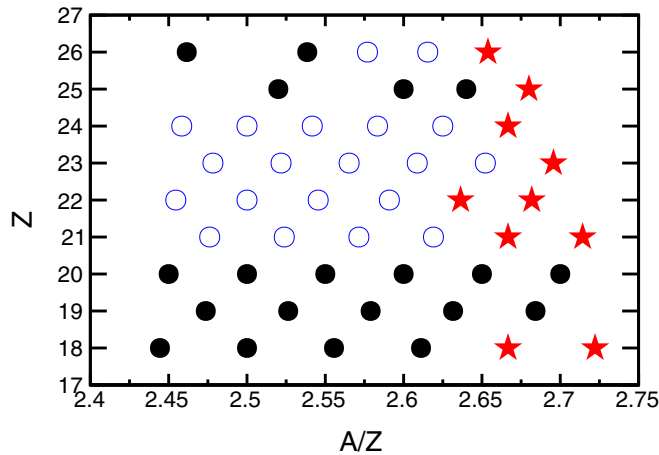

FIG. 9. Map of nuclides observed in the TOF mass measurement (with sufficient statistics to obtain a TOF value) in terms of the atomic mass number–to–nuclear charge ratio A/Z and nuclear charge Z. Filled black circles indicate reference nuclides, open blue circles indicate nuclides with masses known in the literature, but not to a sufficient precision to qualify as reference nuclides, and red stars indicate nuclides with an unknown mass prior to this experiment. The isotopes ^{63}Mn and ^{63,65}Fe were not considered, as they have known low-lying isomers that preclude these nuclides as calibrants of the mass fit. Our results for $Z = 18$ and $Z = 21$ are published in Refs. [13] and [19], respectively. Our results for $Z = 25$ and $Z = 26$ will be the subject of a forthcoming publication.
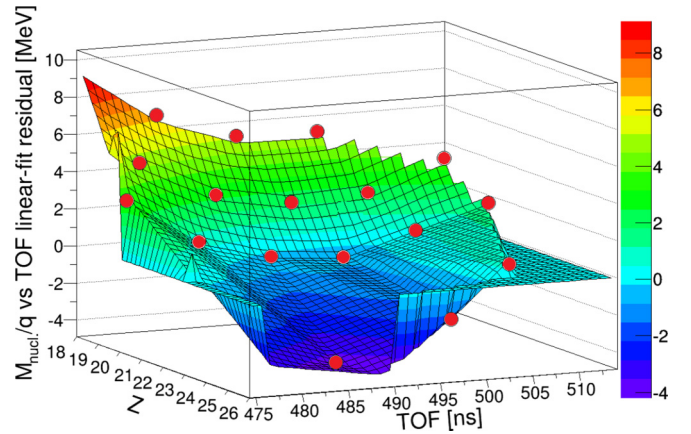

FIG. 10. $m_{\rm rest}/q$–TOF surface of reference nuclides, where the linear dependence of mass over charge m/q on TOF has been removed. Filled red circles mark the nuclear charge Z and TOF of reference nuclides, while the color of the surface at that location indicates the linear fit residual (in MeV). Note that the flat region present outside of the region bounded by data points is a feature of the plotting software.

Since the relationship between mass and TOF at the precision level required to make a meaningful mass measurement was *a priori* unknown, several fit functions were tried, each of which was a combination of polynomials in TOF, nuclear charge Z, and/or a combination of these variables. The goal of this approach was to find the minimum number of terms that reproduce the calibration mass surface without any systematic trends in the fit residuals. This ensures maximum robustness against interpolation and small-distance extrapolation. The complex nature of the $m_{\rm rest}/q$–TOF surface (see Fig. 10) clearly necessitated higher orders in both TOF and Z. A step-by-step procedure was taken to justify the inclusion of each term added to the mass-fit function. To be included in the fit function, an extra term had to significantly reduce the fit residuals and not introduce any systematic trends. The final mass-fit function which was chosen represents the minimal set of terms that minimizes the overall residual-to-literature masses of the 20 reference nuclides and resulted in no detectable systematic biases (i.e., trends in the mass-fit residuals). As might be expected, some degeneracy existed as to the benefit of including certain terms in the fit function. This set of "best" fits was used to inform the uncertainty of masses evaluated from the mass-fit function present from extrapolation from and interpolation between the mass-fit calibration points (see Sec. III C.).

The final mass-fit function employed for the mass results was

$$\frac{m}{q}(\tau) = a_0 + a_1\tau + a_2 z + a_3\tau^2 + a_4 z^2 + a_5 z\tau + a_6 z^4, \quad (5)$$

where a_i are fit parameters. The optimum mass-fit function (of the set explored) and the mass results obtained with Eq. (5) were found to be robust with respect to the removal of a subset of reference nuclides from the mass fit [40]. Figure 10 shows Eq. (5) fit to the $m_{\rm rest}/q$(TOF) data for calibration nuclides. The mass-fit residuals for Eq. (5) are shown in Fig. 11.
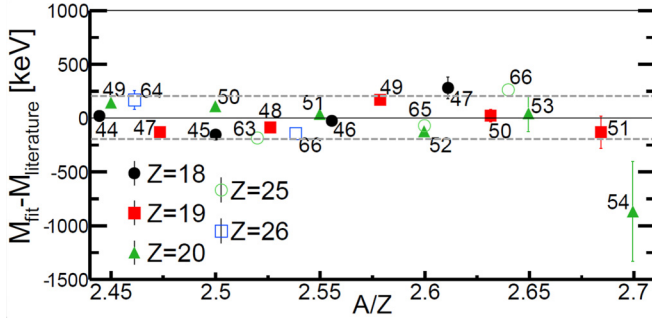
FIG. 11. Residuals of the fit to the m/q(TOF) relationship of calibration nuclides ($^{44-47}$Ar, $^{47-51}$K, $^{49-54}$Ca, ^{63,65,66}Mn, and ^{64,66}Fe) as a function of the mass number–to–nuclear charge ratio A/Z. Error bars indicate statistical uncertainties only. Dashed horizontal gray lines indicate the average systematic mass uncertainty (9 keV/q) included for reference nuclides for the mass fit, as described in Sec. III B.

Equation (5) contains one extra term, $z\tau$, and favors z^4 over z^3 behavior with respect to the previous TOF mass measurement at the NSCL [18]. The z^4 term is only slightly favored over the z^3 term, and a function using the z^3 term instead is included in the set of best-fit functions used to evaluate the extrapolation uncertainty (see Sec. III C.). We surmise that the inclusion of the $z\tau$ term is required due to the extra energy loss induced by the wedge degrader at the intermediate image of the A1900, which was not present in Ref. [18]. This is because $z\tau \propto A$ and, for fixed $B\rho$, energy loss $\Delta E \propto A$ [since $\Delta E \propto Z^2/E$, $E \propto Av^2$, and $(B\rho)^2 = (p/q)^2 \propto ((Av)/Z)^2 = $ constant, where v is the ion velocity and $q = Z$ for the fully stripped ions measured here].

C. Measurement uncertainty

The mass uncertainty for measured nuclides which were not reference nuclides was comprised of a statistical uncertainty determined from the nuclide's individual count rate, the statistically distributed systematic uncertainty which was determined to be present for reference nuclides (and therefore assumed to be present for evaluated nuclides), and two additional uncertainties that were included to account for the uncertainty in the mass-fit function. Namely, these were the uncertainties of the fit coefficients that were a result of the uncertainties in the calibration mass values and TOFs, referred to here as the "Monte Carlo" uncertainty (motivated by the way it was calculated), and the uncertainty from the choice of the general form of the fit function, referred to here as the "function choice" uncertainty.

For the Monte Carlo uncertainty assessment, the mass of each reference nuclide was perturbed by a random amount commensurate with its uncertainty, the mass fit was performed, the fit results were recorded in a histogram, and this perturbation-fit-histogram procedure was repeated 10 000 times. The Monte Carlo uncertainties are the standard deviations of the fit-result mass distributions.

The function choice uncertainty was defined as the difference between the highest and the lowest mass value for

a given nuclide resulting from the set of mass fits that were explored which required a systematic uncertainty less than three times that of the best mass fit to produce a reduced χ^2 equal to 1 and showed no systematic trend in mass-fit residuals. The five fits with six, seven, or eight parameters that were considered for the function choice uncertainty were Eq. (5) and similar functions which contained a z^3 term rather than a z^4 term, lacked the a_6 term altogether, included an additional term that depended on τ^4, and included an additional term that instead depended on $z*\tau^2$. The required statistically distributed systematic uncertainty required for each of these fit functions was 9.0, 11.2, 22.7, 8.5, and 8.2 keV/q. Note that the eight-parameter mass-fit functions were not used in lieu of Eq. (5), as they did not yield a significant reduction in the required systematic uncertainty and thus did not contain the minimal set of terms required to minimize the overall residual to literature masses of the reference nuclides.

Figure 12 shows the statistical [Fig. 12(a)], systematic [Fig. 12(b)], Monte Carlo [Fig. 12(c)], and function choice [Fig. 12(d)] uncertainties of the masses evaluated in this experiment. Their sum in quadrature is shown in Fig. 13. It is apparent that the relative contribution of the uncertainties resulting from the mass-fit extrapolation and interpolation, i.e., the Monte Carlo and function choice uncertainties, becomes larger as the distance of m/q and Z from reference nuclides increases. For the chromium isotopes, which are the focus of this work, the function choice uncertainty dominates, as the Z dependence of the $m_{\rm rest}/q$(TOF) relationship is poorly constrained by the available reference nuclides. New high-precision mass measurements of neutron-rich isotopes of scandium and vanadium would improve this situation.

IV. RESULTS

The atomic mass excesses for the chromium isotopes measured in this experiment are compared to theoretical and literature values in Table I, where we note that the mass of ^{64}Cr was measured for the first time. These results correspond to a mass measurement precision of roughly 1 part in 10^5.

For our mass comparison in Table I we focus on previous experimental values reported [52–54] from the Time-of-Flight Isochronous Spectrometer facility, as these results constitute the primary contribution to the evaluated mass reported for these isotopes in the 2012 AME [29]. We compare them to the theoretical results reported for the 1995 Finite Range Droplet Model (FRDM) [55] and Hartree-Fock-Bogoliubov-21 (HFB-21) [56] since these models are commonly used in astrophysics calculations when experimental data are not available (e.g., Refs. [17,18,57,58]). Additionally, we compare our mass differences to those calculated via the shell model using different interactions and model spaces.

Figure 14 compares the trend in the two-neutron separation energy S_{2n}, $S_{2n}(Z,A) = 2 \times {\rm ME}_{\rm neutron} + {\rm ME}(Z, A - 2) - {\rm ME}(Z, A)$, for neutron-rich isotopes of chromium determined from masses reported in this work to the trends obtained for masses from the 2012 AME [29] and binding energies calculated by the shell model employing the GXPF1A Hamiltonian [59] in the fp shell-model space, as well as shell-model calculations employing a modified version of the
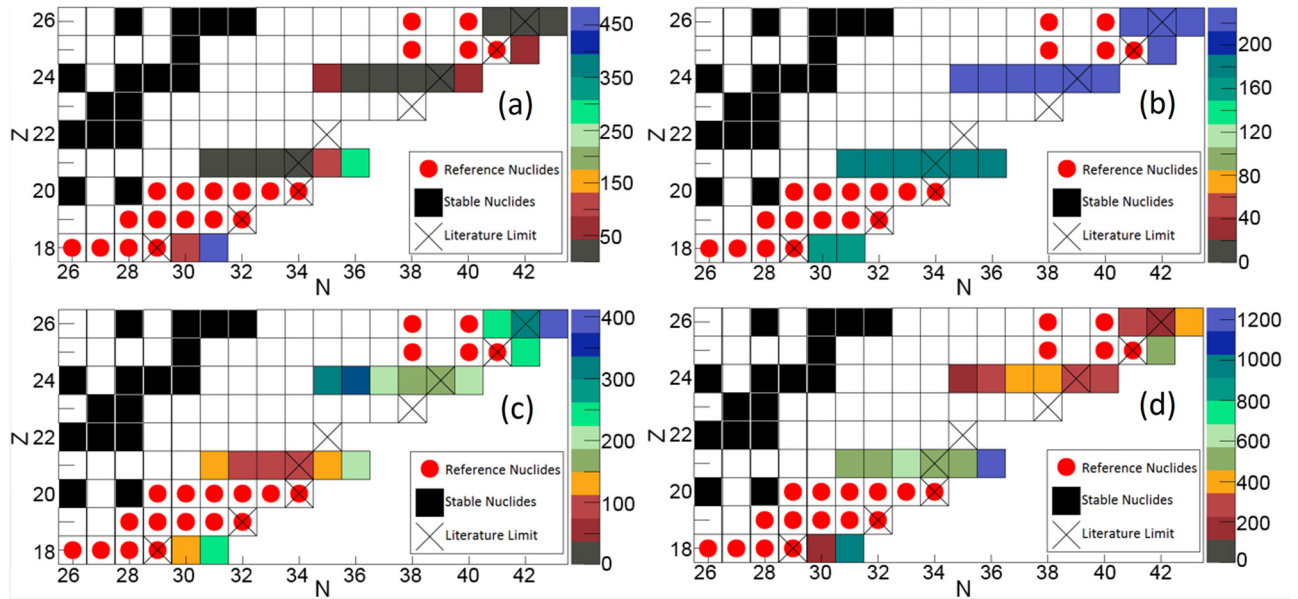
FIG. 12. (a) Statistical, (b) systematic, (c) Monte Carlo, and (d) function choice uncertainties (in keV) for nuclides whose mass was evaluated in this time-of-flight mass measurement. Colored boxes indicate nuclides whose mass was evaluated, with the color reflecting the uncertainty (in keV): boxes with red circles indicate reference nuclides used as calibrants for the m_{rest}/q(TOF) relationship, boxes with X's indicate the most exotic isotope for that element with a known mass prior to this experiment, and black boxes indicate stable nuclides.

Hamiltonian from Ref. [11], which is discussed further in the following section. We note that we extend the S_{2n} trend for the chromium isotopes to $N = 40$ for the first time. The energies of the yrast 2^+ excited states are included in Fig. 14 for comparison, as this trend conveys similar information regarding the evolution of the nuclear structure along the chromium isotopic chain [13].

The discrepancies in experimentally based S_{2n} values, which are largest at $N = 36$ and $N = 38$, primarily stem from the ~650-, ~950-, and ~600-keV differences between this work and the AME values for ^{59}Cr, ^{60}Cr, and ^{61}Cr, respectively. In particular, the difference between our ^{60}Cr mass excess and the adopted AME value causes the S_{2n} trend for $N = 36–38$ to pivot about $N = 37$. As shown in Table I of Ref. [29], the 2012 AME values for these three nuclides
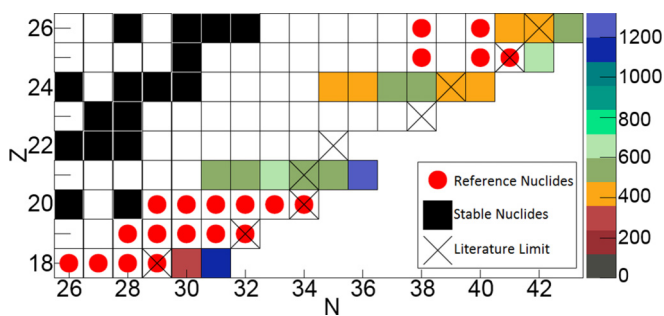

FIG. 13. Same as Fig. 12, but with the color indicating the total uncertainty of the evaluated nuclide (in keV), where the total is the sum in quadrature of the statistical, systematic, Monte Carlo, and function choice uncertainties. Note that ^{56}Sc has an additional systematic uncertainty due to the presence of a β-decaying isomer (see Ref. [19] for more details) which is not included in this figure.

are primarily based on three separate measurements from the Time-of-Flight Isochronous Spectrometer facility [52–54], amongst which there is an ~500-keV discrepancy for the reported masses of ^{59,60}Cr and an ~1700-keV discrepancy for the reported ^{61}Cr masses (see Table I).

V. DISCUSSION

A. Structural evolution of the neutron-rich chromium isotopes

The trend in binding energies determined in this work can be used as a probe of the evolution of shell structure for neutron-rich chromium isotopes [12]. Typically, S_{2n} is employed to isolate the structural changes present along neutron-rich isotopes of an element (e.g., Refs. [7,13,31,48,63]). Along an isotopic chain, S_{2n} generally declines with increasing N away from β stability due to the penalty in binding energy for a large neutron-proton asymmetry, as described by the liquid-drop model. This decline is markedly increased following a nucleus that exhibits a magic neutron number, since the two-neutron removal (addition) required to move from (to) a nucleus with magic N is energetically disfavored (favored) due to the shell gap associated with N_{magic} [12]. A leveling of S_{2n} for a few isotopes, followed by a continuation of the gradually decreasing trend, is a signature of a shape transition along an isotopic chain [64].

The S_{2n} trends in Fig. 14 demonstrate the different structural changes implied by the masses presented in this work and the evaluated masses of the 2012 AME [29]. Our new data disfavor the change in the S_{2n} slope at $N = 36$ shown by the 2012 AME data, instead favoring a continuation of the previous slope until $N = 38$. We note that the flattening of the AME S_{2n} trend about $N = 36$ is more consistent with the identification of ^{60}Cr as the shape-transition point in Ref. [9]. The decrease

TABLE I. Atomic mass excesses (in keV) of chromium isotopes measured in this experiment compared to results from previous direct mass measurements from the Time-of-Flight Isochronous (TOFI) spectrometer (TOFI1 [52], TOFI2 [53], and TOFI3 [54]), the adopted value in the 2012 Atomic Mass Evaluation (AME) [29] ("E" indicates an extrapolated value), and predictions from global mass models (FRDM [55] and HFB-21 [56]).

Isotope	This experiment	AME 2012	TOFI1	TOFI2	TOFI3	FRDM	HFB-21
^{59}Cr	−48540(440)	−47891(244)	−47710(230)	−47850(250)	−47320(310)	−48680	−49160
^{60}Cr	−47440(460)	−46504(213)	−46280(230)	−46830(260)	−46510(280)	−47910	−48200
^{61}Cr	−43080(510)	−42455(129)	−41500(400)	−42770(280)	−42120(280)	−42700	−43710
^{62}Cr	−40890(490)	−40895(148)	−39500(600)	−41200(400)	−40200(350)	−41180	−41960
^{63}Cr	−35940(430)	−35722(459)	. . .	. . .	. . .	−36030	−37290
^{64}Cr	−33480(440)	−33459E(298E)	. . .	. . .	. . .	−34950	−34730

in the magnitude of our S_{2n}-trend slope approaching $N = 40$ is consistent with the collective behavior previously identified in Refs. [5–9]. It is interesting to note that our S_{2n} trend for $^{62-64}$Cr ($N = 38–40$) resembles the trend for $^{30-32}$Mg ($N = 18–20$) [65], where ^{32}Mg marks the entrance of the magnesium isotopic chain into the $N = 20$ island of inversion [66–68]. However, the masses of chromium isotopes with $N > 40$ are required to provide a firm signature of the presence or absence of the $N = 40$ subshell gap for this element.

The striking divergence between the experimental S_{2n} trends and the shell-model-derived trend (GXPF1A) shown in Fig. 14 highlights the need for inclusion of the $g_{9/2}$ and $d_{5/2}$ orbits in order to obtain a realistic description of the chromium isotopes for $N \geqslant 35$, which has been pointed out in previous studies [69–71]. We have thus performed large-scale shell-model calculations within the proton fp and neutron $fpg_{9/2}d_{5/2}$ model space, employing the Hamiltonian from Ref. [11] with minor modifications [72,73]. Additionally, the global monopole term was made more attractive by 30 keV to obtain a better agreement of the S_{2n} energies in neutron-rich chromium and iron isotopes. These refinements preserve the
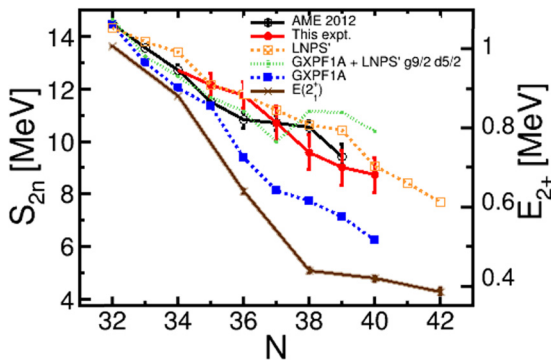

FIG. 14. Two-neutron separation energy S_{2n} for neutron-rich isotopes of chromium as calculated from the 2012 Atomic Mass Evaluation (open black circles) and the masses reported here (filled red circles), as well as by shell-model calculations employing the GXPF1A Hamiltonian [59] (filled blue triangles) and LNPS′ Hamiltonian (modified from Ref. [11]) (open orange squares). The contribution of the $g_{9/2}$ and $d_{5/2}$ orbitals is shown by adding their contribution to the LNPS′ results to S_{2n} calculated with the GXPF1A Hamiltonian (green points). The energies of yrast 2^+ excited states of corresponding isotopes are shown for comparison (brown X's) [5,60–62].

spectroscopy of the nuclides in the island of inversion region presented in Ref. [11].

The results of the calculations with the modified LNPS Hamiltonian, hereafter dubbed the LNPS′, are also presented in Fig. 14. As shown, the agreement is more satisfactory than for the GXPF1A Hamiltonian and the LNPS′ results match the present data within the error bars for the majority of cases. The largest discrepancy is found for the S_{2n} value of ^{63}Cr, which is overestimated. This is surprising, as the present model accurately reproduces the known excitation energies of chromium isotopes, with the visible drop in the yrast 2^+ excited-state energies between $N = 36$ and $N = 38$, indicating that chromium isotopes undergo a shape change at $N = 38$. However, little is known about the spectroscopy of ^{63}Cr [74] and the ground-state spin assignments of both ^{63}Cr and ^{61}Cr are tentative, making it difficult to evaluate whether these nuclides have the correct degree of collectivity in the present shell-model calculations. In spite of this discrepancy, the LNPS′ shell-model trend clearly points to the development of collectivity around $N = 40$ and predicts continuation of the deformation onset towards higher neutron numbers. This increase in collectivity agrees with the recent measurement of the yrast 2^+ excited-state energy for ^{66}Cr [62].

We have also examined the summed occupancies of the neutron intruder orbitals $g_{9/2}$ and $d_{5/2}$ within the LNPS′ model. The contribution of these is shown in Fig. 14, added to the GXPF1A results. The occupation of the neutron intruder orbitals becomes significant at $N = 36$ (∼1.8 particles) and coincides directly with the place where the deviation between GXPF1A calculations and experiment becomes large. Further increase in this occupancy with increasing neutron number (see also Table II in Ref. [11]) explains the failure of shell-model calculations limited to the fp shell-model space to reproduce S_{2n} for the neutron-rich chromium isotopes.

B. $A = 64$ electron-capture heating in the accreted neutron star crust

Heating and cooling due to electron-capture reactions within the accreted neutron star crust have been shown to affect the outer crust thermal profile and the associated astronomical observables [17–19,26,58,76]. Recent calculations with a state-of-the-art multizone x-ray burst model have shown that $A = 64$ nuclides dominate the crust composition for a wide set of astrophysical conditions (and varied nuclear physics assumptions) that are thought to correspond to typical
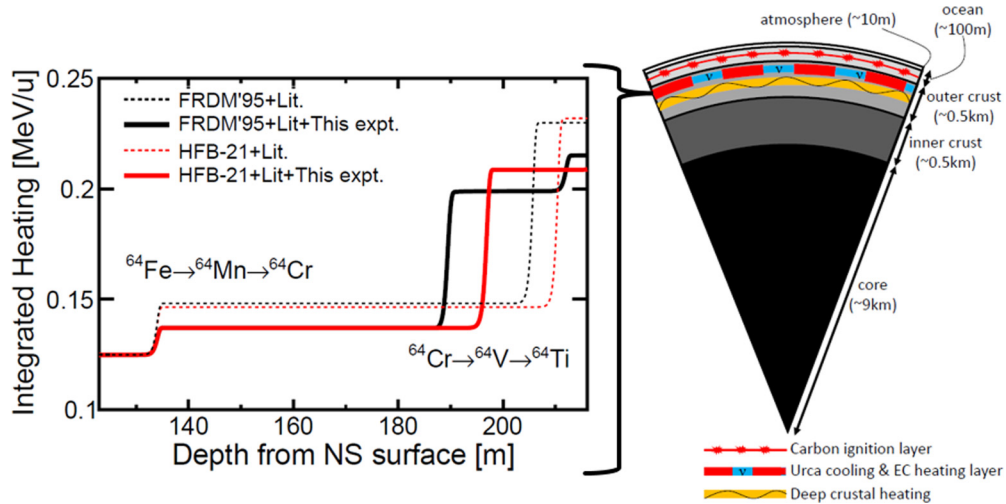
FIG. 15. Integrated heat release (in MeV per accreted nucleon) from electron capture (EC) for an $A = 64$ fluid element as a function of the depth (left panel) in the region where the $^{64}Fe \rightarrow \, ^{64}Mn \rightarrow \, ^{64}Cr$ and $^{64}Cr \rightarrow \, ^{64}V \rightarrow \, ^{64}Ti$ compositional transitions occur, schematically indicated with respect to deep crustal heating [75] and the carbon ignition layer, where x-ray superbursts are powered [24] (right panel), where the neutron star crust nuclear reaction network and quasiparticle random phase approximation Gamow-Teller transition strength distributions reported in Ref. [58] were used. Calculations corresponding to the black and red lines employed the 1995 FRDM [55] and HFB-21 [56] global mass models for nuclides with unknown masses, respectively; the 2012 Atomic Mass Evaluation [29] was used otherwise. Calculations indicated by solid lines include the mass of ^{64}Cr presented here.

x-ray bursting systems [77], and previous work has also demonstrated large $A = 64$ production for stable-burning and superbursting systems [14,16]. In large part due to this prevalence, Ref. [17] identified the $^{64}Cr \rightarrow \, ^{64}V \rightarrow \, ^{64}Ti$ electron-capture sequence as one of the main sources of heat (along with neutron-capture reactions) at the lower extent of the outer crust (i.e., at electron Fermi energy $E_F \geqslant 18.5$ MeV). Though weaker than deep crustal heating sources [75], the shallower depth of this heat source makes it important to consider when calculating the layer at which carbon ignites to power x-ray superbursts, as shown schematically in the right panel in Fig. 15.

We performed calculations with a crust composition evolution model [17,58] in order to assess the impact of our newly measured ^{64}Cr mass on heat release in the accreted neutron star outer crust. The model evolves the composition of an accreted fluid element via nuclear reactions with increasing pressure $p = \dot{m}gt$ (and therefore increasing E_F), where the accretion rate $\dot{m} = 2.64 \times 10^4$ g cm^{-2} s^{-1} ($\approx 0.3 \, \dot{M}_{Eddington}$ for a neutron star of 10-km radius and 1.4 solar masses), surface gravity $g = 1.85 \times 10^{14}$ cm s^{-2}, and time t, at a constant temperature of $T = 0.5$ GK, mimicking the effect of a fluid element being naturally buried in the crust via subsequently accreted material. The crust temperature corresponds to the equilibrium value calculated in Ref. [17] and the astrophysical conditions are within the range inferred for the present population of observed formerly accreting cooling neutron stars [78]. The nuclear reaction network includes electron capture, β decay, neutron capture and emission, and fusion reactions.

The resultant integrated nuclear energy release profiles as a function of the depth into the neutron star from our calculations are shown in Fig. 15 using our ^{64}Cr mass and the ^{64}Cr masses from the commonly used global mass models FRDM'95 [55]

and HFB-21 [56]. The >1-MeV reduction in binding we observe for ^{64}Cr with respect to FRDM and HFB-21, an $\sim 3\sigma$ deviation using our experimental uncertainty, results in a substantially reduced odd-even mass staggering for both the Fe-Mn-Cr and the Cr-V-Ti $A = 64$ sequences, which reduces the heat release from both electron-capture sequences [17,19]. Additionally, the reduced ^{64}Cr binding energy leads to an earlier transition to ^{64}Cr and therefore a shallower depth for the heat deposition from the $^{64}Cr \rightarrow \, ^{64}V \rightarrow \, ^{64}Ti$ electron-capture sequence. We note, however, that the masses of ^{64}V and ^{64}Ti must be experimentally determined to confirm our conclusions for this second electron-capture sequence.

VI. CONCLUSIONS

We performed time-of-flight nuclear mass measurements of the $A = 59$–64 isotopes of chromium at the NSCL at Michigan State University, where the mass of ^{64}Cr was determined for the first time. Our results demonstrate a different behavior with respect to the 2012 AME for the S_{2n} trend in the chromium isotopes approaching $N = 40$, indicating that the shape transition from spherical to deformed begins at $N = 38$ rather than $N = 36$. This S_{2n} trend difference is primarily due to the discrepancy between our measured and the 2012 AME evaluated masses for $^{59-61}Cr$. Our ^{64}Cr mass extends the S_{2n} trend for the chromium isotopes to $N = 40$ for the first time, revealing a trend in mass systematics which is consistent with the previously inferred collective behavior of chromium in this region. We find a reduction in binding energy for ^{64}Cr of 1.47 and 1.25 MeV with respect to the global mass models FRDM'95 and HFB-21, respectively, which are commonly used in astrophysics simulations. Based on our experimental mass uncertainty, these differences correspond

to an $\sim 3\sigma$ deviation. This reduction in binding energy leads to a reduced odd-even mass stagger near chromium in the $A = 64$ isobaric chain, ultimately causing a reduction of the magnitude and depth of electron-capture heating associated with ^{64}Cr, a major heat source in the outer crust of accreting neutron stars. Additionally, we performed state-of-the-art shell-model calculations to calculate S_{2n} for the chromium isotopic chain, demonstrating the importance of including the $g_{9/2}$ and $d_{5/2}$ neutron valence spaces for shell-model calculations in this region. Future high-precision (e.g., Penning trap) mass measurements of scandium and vanadium isotopes in this region will enable a reevaluation of the presented data,

likely reducing the systematic uncertainty of our chromium masses. In order to conclusively determine the magnitude of electron-capture heating in the $A = 64$ isobaric chain, the masses of ^{64}V and ^{64}Ti will need to be measured.

[1] B. A. Brown, Prog. Part. Nucl. Phys. **47**, 517 (2001).

[2] R. V. F. Janssens, Phys. Scripta **T152**, 014005 (2013).

[3] J. Erler *et al.*, Nature (London) **486**, 509 (2012).

[4] O. Sorlin *et al.*, Eur. Phys. J. A **16**, 55 (2003).

[5] A. Gade *et al.*, Phys. Rev. C **81**, 051304(R) (2010).

[6] T. Baugher *et al.*, Phys. Rev. C **86**, 011305(R) (2012).

[7] S. Naimi *et al.*, Phys. Rev. C **86**, 014325 (2012).

[8] H. L. Crawford *et al.*, Phys. Rev. Lett. **110**, 242701 (2013).

[9] T. Braunroth *et al.*, Phys. Rev. C **92**, 034306 (2015).

[10] P. Adrich, A. M. Amthor, D. Bazin, M. D. Bowen, B. A. Brown, C. M. Campbell, J. M. Cook, A. Gade, D. Galaviz, T. Glasmacher, S. McDaniel, D. Miller, A. Obertelli, Y. Shimbara, K. P. Siwek, J. A. Tostevin, and D. Weisshaar, Phys. Rev. C **77**, 054306 (2008).

[11] S. M. Lenzi, F. Nowacki, A. Poves, and K. Sieja, Phys. Rev. C **82**, 054301 (2010).

[12] D. Lunney, J. M. Pearson, and C. Thibault, Rev. Mod. Phys. **75**, 1021 (2003).

[13] Z. Meisel *et al.*, Phys. Rev. Lett. **114**, 022501 (2015).

[14] H. Schatz, L. Bildsten, A. Cumming, and M. Wiescher, Astrophys. J. **524**, 1014 (1999).

[15] H. Schatz *et al.*, Phys. Rev. Lett. **86**, 3471 (2001).

[16] H. Schatz, L. Bildsten, and A. Cumming, Astrophys. J. Lett. **583**, L87 (2003).

[17] S. Gupta, E. F. Brown, H. Schatz, P. Möller, and K.-L. Kratz, Astrophys. J. **662**, 1188 (2007).

[18] A. Estradé *et al.*, Phys. Rev. Lett. **107**, 172503 (2011).

[19] Z. Meisel *et al.*, Phys. Rev. Lett. **115**, 162501 (2015).

[20] S. E. Woosley and R. E. Taam, Nature (London) **263**, 101 (1976).

[21] H. Schatz and K. Rehm, Nucl. Phys. A **777**, 601 (2006).

[22] A. Parikh, J. José, G. Sala, and C. Iliadis, Prog. Part. Nucl. Phys. **69**, 225 (2013).

[23] A. Cumming and L. Bildsten, Astrophys. J. Lett. **559**, L127 (2001).

[24] L. Keek, A. Heger, and J. J. M. in 't Zand, Astrophys. J. **752**, 150 (2012).

[25] E. F. Brown and A. Cumming, Astrophys. J. **698**, 1020 (2009).

[26] A. Deibel, A. Cumming, E. F. Brown, and D. Page, Astrophys. J. Lett. **809**, L31 (2015).

[27] L. Bildsten, Astrophys. J. Lett. **501**, L89 (1998).

[28] G. Ushomirsky, C. Cutler, and L. Bildsten, Mon. Not. R. Astron. Soc. **319**, 902 (2000).

[29] G. Audi, M. Wang, A. Wapstra, F. Kondev, M. MacCormick, X. Xu, and B. Pfeiffer, Chin. Phys. C **36**, 1287 (2012).

[30] Z. Meisel and S. George, Int. J. Mass Spectrom. **349-350**, 145 (2013).

[31] L. Gaudefroy *et al.*, Phys. Rev. Lett. **109**, 202503 (2012).

[32] M. Matoš *et al.*, Nucl. Instrum. Methods Phys. Res. Sec. A **696**, 171 (2012).

[33] D. J. Morrissey, B. M. Sherrill, M. Steiner, A. Stolz, and I. Wiedenhoever, Nucl. Instrum. Methods Phys. Res. Sec. B **204**, 90 (2003).

[34] D. Bazin, J. Caggiano, B. Sherrill, J. Yurkon, and A. Zeller, Nucl. Instrum. Methods Phys. Res. Sec. B **204**, 629 (2003).

[35] J. Yurkon *et al.*, Nucl. Instrum. Methods Phys. Res. Sec. A **422**, 291 (1999).

[36] R. York *et al.*, in *Cyclotrons and Their Applications 1998: Proceedings of the Fifteenth International Conference on Cyclotrons and Their Applications, Caen, France, 1–19 June 1998*, edited by E. Baron and M. Liuvin (Institute of Physics, Philadelphia, PA, 1999), pp. 687–691.

[37] Saint-Gobain Crystals; http://www.crystals.saint-gobain.com.

[38] Hamamatsu Photonics; http://www.hamamatsu.com.

[39] Belden CDT Inc.; http://www.belden.com.

[40] Z. Meisel, Ph.D. thesis, Michigan State University, East Lansing, 2015.

[41] D. Shapira, T. Lewis, and L. Hulett, Nucl. Instrum. Methods Phys. Res. Sec. A **454**, 409 (2000).

[42] Quantar Technology Inc.; http://www.quantar.com.

[43] Magnet Sales and Manufacturing Inc.; http://www.magnetsales.com.

[44] M. Jung, H. Rothard, B. Gervais, J.-P. Grandin, A. Clouvas, and R. Wünsch, Phys. Rev. A **54**, 4153 (1996).

[45] L. Landau and E. Lifshitz, *The Classical Theory of Fields*, 4th ed. The Course of Theoretical Physics, Vol. 2 (Elsevier, Amsterdam, 1975).

[46] A. M. Rogers *et al.*, Nucl. Instrum. Methods Phys. Res. Sec. A **795**, 325 (2015).

[47] ROOT Data Analysis Framework; https://root.cern.ch/drupal/.

[48] F. Wienholtz *et al.*, Nature (London) **498**, 346 (2013).

[49] National Nuclear Data Center compilation; http://www.nndc.bnl.gov/. Accessed January 2014.

[50] W. Lotz, J. Opt. Soc. Am. **60**, 206 (1970).

[51] L. Chen *et al.*, Nucl. Phys. A **882**, 71 (2012).

[52] X. Tu *et al.*, Z. Phys. A **337**, 361 (1990).

[53] H. Seifert *et al.*, Z. Phys. A **349**, 25 (1994).

[54] Y. Bai, D. J. Vieira, H. L. Seifert, and J. M. Wouters, AIP Conf. Proc. **455**, 90 (1998).

[55] P. Möller, J. Nix, W. Myers, and W. Swiatecki, At. Data Nucl. Data Tables **59**, 185 (1995).

[56] S. Goriely, N. Chamel, and J. M. Pearson, Phys. Rev. C **82**, 035804 (2010).

[57] J. M. Pearson, S. Goriely, and N. Chamel, Phys. Rev. C **83**, 065810 (2011).

[58] H. Schatz *et al.*, Nature (London) **505**, 62 (2014).

[59] M. Honma, T. Otsuka, B. A. Brown, and T. Mizusaki, Eur. Phys. J. A **25**, 499 (2005).

[60] S. Raman, C.W. Nestor Jr., and P. Tikkanen, At. Data Nucl. Data Tables **78**, 1 (2001).

[61] N. Mărginean *et al.*, Phys. Lett. B **633**, 696 (2006).

[62] V. Werner *et al.*, Eur. Phys. J. Web Conf. **107**, 03007 (2016).

[63] M. Rosenbusch *et al.*, Phys. Rev. Lett. **114**, 202501 (2015).

[64] F. Iachello, A. Leviatan, and D. Petrellis, Phys. Lett. B **705**, 379 (2011).

[65] A. Chaudhuri *et al.*, Phys. Rev. C **88**, 054317 (2013).

[66] B. V. Pritychenko *et al.*, Phys. Lett. B **461**, 322 (1999).

[67] J. R. Terry *et al.*, Phys. Rev. C **77**, 014316 (2008).

[68] K. Wimmer *et al.*, Phys. Rev. Lett. **105**, 252501 (2010).

[69] A. Deacon *et al.*, Phys. Lett. B **622**, 151 (2005).

[70] S. Zhu *et al.*, Phys. Rev. C **74**, 064315 (2006).

[71] T. Togashi, N. Shimizu, Y. Utsuno, T. Otsuka, and M. Honma, Phys. Rev. C **91**, 024320 (2015).

[72] E. Sahin *et al.*, Phys. Rev. C **91**, 034302 (2015).

[73] P. Morfouace *et al.*, Phys. Lett. B **751**, 306 (2015).

[74] S. Suchyta *et al.*, Phys. Rev. C. **89**, 034317 (2014).

[75] A. W. Steiner, Phys. Rev. C **85**, 055804 (2012).

[76] A. Deibel, Z. Meisel, H. Schatz, E. F. Brown, and A. Cumming, arXiv:1603.01281.

[77] R. H. Cyburt, A. M. Amthor, A. Heger, E. Johnson, Z. Meisel, H. Schatz, and K. Smith, forthcoming (2016).

[78] A. Turlione, D. N. Aguilera, and J. A. Pons, Astron. Astrophys. **577**, A5 (2015).